Mechanical organization yields degenerate dissipation beyond linear response

Zachary Gao Sun[1,2,3,4], Juanjuan Zheng[4], A. Pasha Tabatabai[2,5], Joost J. Vlassak[4], and Michael Murrell[1,2,3,5, *]

[1] Department of Physics, Yale University, 217 Prospect Street, New Haven, Connecticut 06511, USA

[2] Systems Biology Institute, Yale University, 850 West Campus Drive, West Haven, Connecticut, 06516, USA

[3] Integrated Graduate Program in Physical and Engineering Biology, Yale University, New Haven, Connecticut 06520, USA

[4] John A. Paulson School of Engineering and Applied Sciences, Harvard University, Cambridge, MA, USA

[5] Department of Biomedical Engineering, Yale University, 55 Prospect Street, New Haven, Connecticut 06511, USA

[*]Corresponding author. Email address: michael.murrell@yale.edu .

Abstract

In non-equilibrium (active) systems, increased driving is commonly assumed to amplify energy dissipation. This frames the efficiency of protein-based machines as a fixed or monotonically decreasing function with driving. Using picowatt-sensitive calorimetry and advanced entropy production metrics in reconstituted actomyosin networks, we show that energy dissipation depends non-monotonically on myosin-generated stress (driving). At low driving, dissipation increases proportionally with stress, consistent with near-equilibrium linear response. At high driving, however, dissipation decreases, revealing a far-from-equilibrium regime in which excessive load suppresses motor ATPase activity. This non-monotonicity reflects a transition from spatially localized stress at low driving to delocalized stress at high driving, where force per motor, and thus ATPase suppression, is maximized. Crosslinker mechanics tune this transition as fascin (slip bonds) amplifies stress localization and shifts the dissipation peak to higher driving, whereas α-actinin (catch bonds) stabilizes under load, delocalizes stress, and shifts the peak to lower driving. Thus, enhanced mechanochemical coupling causes additional driving to restructure rather than amplify dissipation, revealing how material system organization (bonding), and not driving alone, governs energy flow far from equilibrium.

Main Text

Introduction

In non-equilibrium systems, increased driving is commonly assumed to amplify energy dissipation, reflecting the conventional assumption inherited from linear response and irreversible thermodynamics [1-5]. This intuition links activity, force generation, and energetic cost, in that stronger driving produces larger fluxes and greater heat loss. It underlies how efficiency is typically understood in systems ranging from molecular machines to active solids, where enhanced activity is often equated with increased dissipation. Whether this assumption remains valid when the system is driven far from thermodynamic equilibrium, however, remains largely unexplored.

Linear response theory predicts that fluxes scale proportionally with their conjugate forces and that entropy production increases monotonically with driving[1,6-10]. In this regime, dissipation is determined by transport coefficients that are independent of the applied force, and added input is converted directly into heat through Onsager reciprocity[6]. This framework has been remarkably successful in describing transport[11] and pattern formation in passive matter[12], and is often implicitly extended to active systems[13-16]. Active materials, however, operate far from equilibrium, where driving does not merely induce motion but impacts the material itself[13,14,16]. In the cell cytoskeleton for example, internally generated stresses alter connectivity, stiffness, and force transmission, introducing feedback between mechanical organization and energy consumption. Among these feedbacks include load-dependent bonds [17-20], which endow the cytoskeleton with adaptability, in the ability to transition between solid-like and fluid-like states through motor-generated stresses transmitted by filamentous networks[21-24]. In such systems, dissipation may no longer be set by driving alone, but how the system redistributes or allocates energy across internal degrees of freedom. Directly testing this possibility has been challenging, in part because energy dissipation is rarely measured alongside material organization. As a result, it remains unclear whether dissipation in active matter necessarily increases with driving, or whether it can instead be regulated by the internal organization of the material.

Here we show that increased driving does not necessarily amplify dissipation in active materials but instead reorganizes how energy is dissipated through stress localization and delocalization. To this end, we use the actomyosin cytoskeleton as a model non-equilibrium material, where myosin motors consume chemical energy (ATP) and through the generation of active stress, drive the cytoskeleton beyond the linear regime[22-26]. As a function of driving, mechano-sensitive bonds introduce feedback between mechanical force transmission and chemical (ATPase) activity, determining material organization (e.g. crosslinking), stress focusing and a non-monotonic dissipation of energy. The impact of the bonds are twofold: catch bonds (α-actinin) strengthen under tensile load[21,27-30], stabilizing stressed networks, whereas slip bonds (fascin) unbind under increased tension[31,32], shifting the peak in dissipation to different driving, and fine tuning stress concentration akin to Anderson Localization in amorphous materials. Thus, by reconstituting 2D and 3D actomyosin networks with defined bond mechanics, we demonstrate that dissipation does not increase monotonically with driving and directly link non-monotonic behavior to a material transition between stress localization and delocalization[33,34]. Combining confocal fluorescence microscopy, entropy production, picowatt-sensitive calorimetry, and rheology, we show how mechanochemical feedback reshapes energy flow in active matter, revealing mechanisms by which driving reorganizes, rather than simply amplifies dissipation in a far from equilibrium regime.

Results

We assemble model actomyosin networks in two configurations [35]. First, we assemble a quasi-2D network, amenable for fluorescence imaging and the quantification of filament dynamics [36-38]. Second, we assemble a 3D network, more amenable to rheology[39-42] and calorimetry (Methods). Integrating 3D imaging with pico-calorimetry allows direct comparison of network local deformation and heat dissipation, while rheological measurements provide complementary mechanical characterization. The molar ratios of proteins (e.g., crosslinker-to-actin and myosin-to-actin) are identical in the 2D and 3D assays, although the use of a crowding agent in the 2D system results in higher effective surface protein concentrations compared to bulk concentrations in 3D networks that are without crowding agent.

Catch- and slip-bond networks are mechanically indistinguishable under thermal fluctuations but diverge under active stress.

We reconstitute a quasi-two-dimensional active actomyosin network by confining pre-polymerized actin filaments to a supported lipid bilayer using 0.25% methylcellulose, crosslinking the network with fascin or α-actinin, as fascin is known to be a slip bond, while α-actinin is a catch bond [21](Fig. 1a). We then introduce skeletal muscle myosin II to generate active contractile stress (Fig. 1a). Under high crosslinker density ($R_c > 0.2$), pseudo-2D α-actinin and fascin crosslinked network sheets are morphologically indistinguishable (Fig1 b-d). Both α-actinin and fascin crosslink and bundle F-actin into thick bundles (Fig. d-e). Under thermal driving force, F-actin networks crosslinked by α-actinin and fascin exhibit similar relaxation time, suggestive of comparable rigidity (Fig1. f-g). However, the dynamics of the networks crosslinked by α-actinin and fascin are distinctively different under myosin-induced active stress: fascin-crosslinked networks contract locally into asters (Fig. 1h, supplementary movie 1); in contrast, α-actinin-crosslinked networks behave as cohesive elastic sheets that rupture via crack formation[38] (Fig. 1h-i, supplementary movie 1). The distinct contractile behaviors of the two crosslinked networks lead to differences in both the magnitude of strain and the time to material failure. (Fig. 1j-k). We hypothesize the difference in the mechanical dynamics of the two types of networks is due to the difference in bond mechano-sensitivity and mechanics[21] (Supplemental Materials). Therefore, due to the opposite mechanism of bond kinetics under load, slip bonds tend to unbind in high-stress regions while catch bonds tend to unbind in low-stress regions. This results in potentially the homogenization of stress in the α-actinin-crosslinked network which enables the active material to endure higher stress. Interestingly, in α-actinin crosslinked networks, the strain rate of deformation exhibits a non-monotonic dependence on myosin concentration, with strain rate peaks at around $R_{myo} \approx 0.02$ (Fig. 1l). This unique observation of the dynamics and non-monotonicity in the nonlinear/contractile regime is reminiscent of mechanical inhibition of dissipation in active solids[43]. Therefore, to investigate the origin of the non-monotonicity, we begin to investigate the energy partition and heat dissipation of the networks under active stress.

Mechano-chemical coupling yields non-monotonic dissipation with driving

We reconstitute a three-dimensional active actomyosin network by mixing purified G-actin, skeletal muscle myosin II, and crosslinkers such as α-actinin or fascin with ATP in F-buffer (Methods). This protein mixture was injected into a glass capillary tube mounted inside a custom-built picowatt-calorimeter. The calorimeter achieves a lower detection limit of 85 pW (Fig. 2a, SFig. 1, Methods) [Zheng et al., In submission]. The total heat dissipation results from

predominantly three mechanisms: 1) ATP hydrolysis of actin polymerization, 2) ATPase kinetics via myosin motors, and 3) ATP regeneration system via pyruvate kinase and lactic dehydrogenase (PK-LDH) along with phosphoenolpyruvate (PEP) (Fig. 2b, SFig. 1, Methods). Upon polymerization, heat dissipation from the F-actin network was captured and exhibited an exponential decay over time, consistent with prior work on actin polymerization kinetics[44] (Fig. 2c-d, Supplementary Materials). We directly measure the heat dissipation ΔQ, and each data point is collected every 0.5 seconds, results in heat dissipation per unit time (power), $\dot{Q} = \Delta Q/\Delta t$. After characterizing the heat dissipation of actin polymerization, we introduce skeletal muscle myosin II dimers into the protein mix, which performs power strokes on F-actin and causes network deformation and contraction[45] (Supplementary Materials). We increase ATP concentration while keeping actin and myosin concentration constant, the measured heat dissipation rate $\dot{Q}$ follows Michaelis–Menten kinetics:

$$J_{ATPase}([ATP]) = \frac{k_{cat}^{ATP}[ATP]}{K_M^{ATP} + [ATP]}[M]_{tot} \quad (1)$$

, where K_M^{ATP} = 0.1397 $\pm$ 0.09345 μM , of which the difference is within a factor of 2 compared to values from previous studies[46] (Fig. 2e), potentially due to the differences in actin concentration and myosin motor type. We then vary the concentration of actin, and the heat dissipation rate $\dot{Q}$ also follows Michaelis–Menten kinetics:

$$J_{ATPase}([A]) = \frac{k_{cat}[ATP]}{K_A + [ATP]}[M]_{tot} \quad (2)$$

, where $K_A = 13.11 \pm 9.6125$ μM, agrees with previous work[47,48] (Fig. 2f).

To further investigate the energetic role of motor activity, we systematically varied the myosin concentration while maintaining a constant actin concentration. The heat dissipation profile of the resulting actomyosin networks exhibits a non-monotonic trend as myosin concentration increases (Fig. 2g). We hypothesize that above a critical myosin-to-actin molar ratio (R_{myo} > 0.02), the network enters a highly connected regime in which active stresses become uniformly distributed due to myosin's mechanosensitivity. In this regime, myosin thick filaments can behave as catch bonds, and therefore the ATPase activity of myosin is reduced due to increased mechanical load across the network[49-52], reflected as a decreased rate of heat dissipation (Fig. 2g). This is reminiscent of the non-monotonicity of dissipation observed in 'active solids' as in our contractile 2D-network experiments (Fig. 1), in which energy dissipation peaks at intermediate stress and is inhibited at large tensile or compressive loads[43]. The nuance between the 2D system and 3D system is that the 3D system does not exhibit large scale deformation, potentially due to geometry and the effective protein concentration differences (Fig. 2g, supplementary movie 2). In our case, the heat dissipation primarily comes from the ATPase activity and ATP regeneration system (SFig. 1, Supplemental Materials). The heat dissipation is linearly proportional to the concentration (number) of myosin head performing ATPase, c_{head} , the myosin ATPase rate, r (s^{-1}), the volume of the chamber, V (80 nL in this case), and ΔG, the free energy, which is ≈ 60 kJ/mol. The heat dissipation rate $\dot{Q}$ measured then follows:

$$\dot{Q} = \Delta Q/\Delta t = c_{head} \cdot r \cdot V \cdot \Delta G \quad (3)$$

.

From this, we can calculate an effective myosin ATPase rate (SFig. 2, Supplemental Materials), which can indirectly infer the level of active stress, σ_a, experienced by the motors since myosin ATPase rate r is inversely proportional to active stress σ_a[49-51,53].

To elucidate how differences in force sensing and mechano-sensitive binding shape energetic output, we examine actin networks crosslinked with either α-actinin (catch bond) or fascin (slip bond) using 3D microscopy and pico-calorimetry. This allows us to directly compare how distinct bond mechanics influence stress generation and heat dissipation under active motor loading.

Catch bond crosslinked network dissipates more heat under active stress

As mentioned previously, the 3D networks exhibited minimal large-scale deformation under equivalent myosin density, likely due to geometric constraints and effective protein concentrations, as noted in prior studies[26,54] (Fig. 2g). Given the differences in mechanical response between α-actinin and fascin networks under active loading, we next quantify the total heat dissipation of these systems using picowatt-resolution calorimetry.

Under fixed crosslinking and myosin density, increasing the ratio between α-actinin to fascin ($\Phi_{actinin:fascin}$) results in an increase in heat dissipation, potentially due to an elevated ATPase rate with higher $\Phi_{actinin:fascin}$ (Fig. 2h).

To further investigate this behavior, we systematically vary the concentration of myosin motors while maintain constant crosslinker density. In both α-actinin and fascin networks, heat dissipation display a non-monotonic trend as a function of motor density (Fig. 2i). However, the dissipation peak occurred at a higher myosin concentration in fascin networks compared to α-actinin networks (Fig. 2i). Notably, the dissipation curve for the α-actinin case closely resembles that of a network lacking crosslinkers (Fig. 2i), supporting the hypothesis that myosin exhibits catch bond–like behavior. In contrast, the delayed peak observed in fascin networks is likely due to fascin's polarity-sorting capacity and slip bond properties, which restrict stress redistribution until the motor density reaches a threshold where catch bond dynamics begin to dominate (Fig. 2i). Having established that bond mechanics influence how stress accumulates and relaxes, we next ask how these differences translate into measurable changes in energy dissipation.

Therefore, we explore how heat dissipation depends on crosslinking density. For fascin, we observe a sharp drop in dissipation around $R_c \approx 0.001$, near the expected bundling threshold and percolation critical point for 3D networks[41] (Fig. 2j). In contrast, heat dissipation in α-actinin-crosslinked networks remain relatively stable with only a modest decline as R_c increased (Fig. 2j). Across all crosslinker densities, α-actinin networks exhibit higher heat dissipation than fascin networks.

We hypothesize that this is due to α-actinin's catch bond nature, which allows crosslinkers in low-stress regions, where unbinding rates are higher, to relocate to regions of higher stress. This dynamic redistribution promotes stress homogenization across the network[55]. Because myosin ATPase activity is inversely correlated with the mechanical load experienced by motors[49-51,53], the more evenly distributed stress in α-actinin networks may result in higher overall ATP turnover compared to fascin networks, as also shown from the effective ATPase rate calculation (SFig. 2). To directly probe the mechanical stress landscape in these systems and validate this hypothesis, we next perform rheological measurements to characterize the viscoelastic properties of the two network types (Fig. 3a).

Catch bond crosslinked network homogenizes and lowers stress

To characterize the material properties of crosslinked F-actin networks under active stress generated by myosin motors, we use a stress-controlled rheometer (Fig. 3a, Supplementary Materials). Previous studies have suggested that the mechanical response of actively stressed

cytoskeletal networks is analogous to that of passive networks driven into the nonlinear regime via prestress[23,25,56]. Here, we indeed observe that the viscoelastic moduli (G′ and G″) of the network increase with higher R_{myo} (Fig. 3b). This is not due to crosslinking by myosin dimers or thick filaments, as our ATP concentration is within the saturating regime in which myosin dimers have an binding/unbinding time of ~5 ms[23].

In linear frequency sweep experiments, the crossover frequency (ω_{co}), the frequency at which the storage modulus G′ equals the loss modulus G″, serves as a metric for the timescale at which the network transitions from solid-like to fluid-like behavior. More adaptive and transient networks exhibit lower ω_{co} values. At equivalent crosslinking densities, α-actinin–crosslinked networks display significantly lower ω_{co} than fascin-crosslinked ones, indicating more fluid-like and dynamic behavior (Fig. 3c-d). As a control, we also examine networks crosslinked via biotin–streptavidin, a permanent and non-dynamic linkage. Biotin–streptavidin-crosslinked networks display a crossover at very high frequency or almost no crossover, behaving as elastic solids over a wide frequency range (Fig. 3c-d).

As myosin density increases, both G′ and G″ increase monotonically for α-actinin–crosslinked networks, consistent with stress-induced stiffening observed in prior work[23,56] (Fig. 3e-f). In contrast, fascin-crosslinked networks exhibit a non-monotonic response: both moduli initially increased with motor density but later decreased (Fig. 3e-f). This behavior may reflect structural reorganization of the fascin-actin bundles or a mechanical transition from slip bond–dominated to catch bond–dominated dynamics.

To quantify the internal stress exerted by myosin motors, we perform nonlinear rheology on passive networks of matched crosslinking density (Methods). We first apply a step shear prestress σ_0 and allow the sample to reach a quasi-steady state. We then superimpose a small sinusoidal stress $\delta\sigma(t) = |\delta\sigma|e^{i\omega t}$ with amplitude kept within the linear response of the prestressed state ($|\delta\sigma| \leq \sigma_0/10$) so that linear response theory holds[57-59]. The resulting strain response $\delta\gamma(t)$ defines the complex differential modulus as the local slope of the stress–strain relation about σ_0:

$$K^*(\omega, \sigma_0) = \frac{\delta\sigma(\omega)}{\delta\gamma(\omega)}|_{\sigma_0} \tag{4}$$

, with $K'(\omega, \sigma_0) = Re(K^*)$and $K''(\omega, \sigma_0) = Im(K^*)$. In the limit of zero prestress, this reduces to the conventional linear viscoelastic moduli, $K'(\omega, 0) = G'(\omega)$ and $K''(\omega, 0) = G''(\omega)$. We fit the differential elastic modulus with:

$$K'_{pass}(\sigma_0, \omega) = K'_0 + A\,\sigma_0^{\alpha} \tag{5}$$

By extracting the differential elastic modulus K′ as a function of applied prestress, we map the linear moduli (G′, G″) of the active networks onto the stress–stiffening curves of passive ones, thus estimating the active stress imparted by motors (Fig. 3g-h):

$$\sigma_a \approx \left(\frac{(G'_{act} - K'_0)}{A}\right)^{\frac{1}{\alpha}} \tag{6}$$

. At low myosin concentrations, active stress in fascin-crosslinked networks exceed that of α-actinin networks (Fig. 3h). However, above $R_{myo} \approx 0.05$, the active stress in fascin networks decreases. This trend mirrors the calorimetric data (Fig. 2i), in which fascin networks begin to dissipate more heat than α-actinin networks at high motor densities.

We also use velocity information calculated from PIV on 3D network data to extract the mechanical dissipation rate $\langle p_{mech} \rangle$:

$$\langle p_{mech} \rangle = 2\,\beta \int_{0}^{f_{max}} \eta'(2\pi f)\,[\,S_{xx}(f) + S_{yy}(f) + 2\,S_{xy}(f)\,]\,df \tag{7}$$

, in which β is the inverse thermal energy of the bath, $S(f)$ is the power spectral density function for the strain rate (divergence of velocity), and dynamic viscosity $\eta'(2\pi f) = \frac{G''(f)}{2\pi f}$ (Supplemental Materials). We then calculate the mechanical efficiency $\eta = \frac{\langle p_{mech} \rangle}{\langle \dot{Q} \rangle}$, for both slip bond- (fascin) and catch bond- (α-actinin) crosslinked networks. η lies between $5 \times 10^{-5} \sim 1.5 \times 10^{-4}$, with slip bond-crosslinked network showing a higher mechanical efficiency than catch bond-crosslinked network (SFig. 3).

Monotonic increase in driving leads to degeneracy in dissipation

Finally, to elucidate further on the non-monotonic behavior in dissipation due to chemical-mechanical coupling, we perform actin network velocity correlation and entropy production rate analysis[33,34,60] using the actin and myosin fluorescence channel (Methods). The entropy production rate (EPR) provides a lower bound for the dissipation of the system, and further, the thermodynamic molecular details of the system due to mechano-chemical feedbacks. We observe that the EPR exhibit non-monotonic trend as a function of myosin motor concentration, which shows degeneracy at low (R_{myo} = 0.002) and high (R_{myo} = 0.1) driving (Fig. 4 a, d).

Despite their similar dissipation rates, these regimes differ fundamentally in how mechanical stress propagates through the network. Velocity correlation analysis shows that at low myosin activity, stress transmission is short-ranged and localized, whereas at high myosin activity it becomes more delocalized, giving rise to coherent flows across the network (Fig. 4b,c). Thus, comparable entropy production can emerge from distinct stress-propagation modes, demonstrating a degeneracy between dissipation and mechanical organization in active cytoskeletal materials.(R_{myo} = 0.002)

Discussion

Near thermodynamic equilibrium, linear response theory predicts that increasing driving forces lead to a monotonic increase in dissipation: energy fluxes scale linearly with their conjugate forces, and additional input is converted directly into heat through Onsager reciprocity [1,2,7,10,61]. While not an explicit assumption, this expectation is often implicitly extended to active matter, where stronger motor activity is assumed to amplify dissipation[62,63]. Our results demonstrate a fundamental breakdown of this intuition. Instead of monotonically increasing, energy dissipation peaks at intermediate driving and is suppressed at high stress. This non-monotonicity reflects a far-from-equilibrium regime in which added energy is not dissipated more strongly, but reallocated through feedback between mechanical stress, bond kinetics, and motor chemistry. Such behavior is inaccessible to linear response and reveals that, in active materials, driving can restructure pathways of energy flow rather than simply increase entropy production. These results may be potentially a general feature of active systems. While previous work could not statistically distinguish between saturation and modest decrease[64], the non-monotonicity may arise robustly from mechanochemical feedback between stress organization and motor activity.

The physical manifestation of this energetic reallocation is a transition in how mechanical stress is organized in space analogous to Anderson localization in disordered media[65,66]. Rather than remaining uniformly distributed, active stress either concentrates into localized domains or is delocalized across the network, depending on bond mechano-sensitivity (Fig. 4e). Stress focusing

amplifies local force per motor, suppressing ATP turnover and limiting dissipation, whereas stress defocusing distributes load over many motors, sustaining higher chemical flux and elevated heat production. This stress-organization transition provides a concrete, mesoscale mechanism linking microscopic mechanochemistry to macroscopic thermodynamics: dissipation is regulated not by the magnitude of driving alone, but by how that driving is partitioned across space. In this sense, stress localization acts as a control variable for energy flow in active matter. The impact of stress localization is not only to alter the propensity for mechanical propagation, but also in the induction of other active processes, such as transforming mechanical structure into a regulator of metabolic cost.

Non-monotonic behaviors in system variables are ubiquitous and diverse[67,68]. These behaviors can arise from feedback between system variables, such as reactant and product concentration, or through mechanical effects, such as contractions that alter the flow and concentration of chemical species[69]. However, the mechanisms do not necessarily impact thermodynamic forces, such as the ab initio injection of energy. Here, we demonstrate that chemical energy is not a bath, but a subsystem.

Collective organization is known to qualitatively reshape dissipation in condensed-matter systems[70-72]. Calorimetry reveals that networks crosslinked with α-actinin dissipate more heat than those crosslinked with fascin under comparable connectivity and active stress, indicating that stabilizing a stressed cytoskeleton can be more energetically demanding than contracting it. Unlike in superconductors where coherence suppresses dissipation[71,73], the actomyosin network represents an inverted dissipative Bardeen-Cooper-Schrieffer (BCS) system: collective stress homogenization increases the density of active mechanochemical cycles, amplifying energy flux until feedback through bond stabilization suppresses it at high stress.

Figures

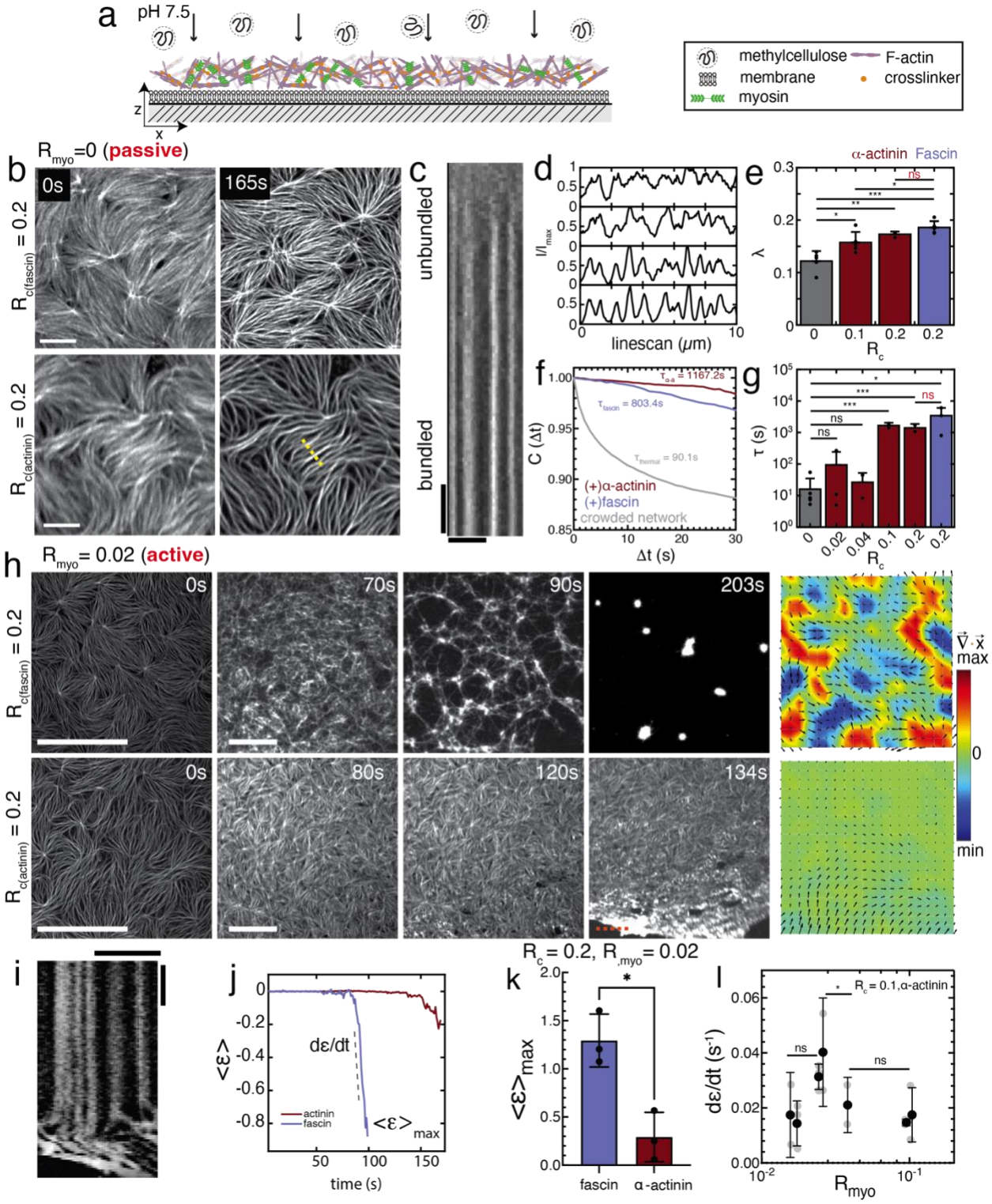

Fig. 1 Activity reveals divergent mechanical responses of catch- and slip-bond crosslinked networks. (a) Schematic of pseudo-2D actomyosin network crowded by Methylcellulose on the lipid bilayer. (b) Confocal fluorescence microscopy image of pseudo-2D actomyosin network crosslinked by fascin (top) and α-actinin (bottom) on a supported lipid bilayer. Left is before

crosslinking, and right is post crosslinker addition. Scalebar is 5 µm. (c) Kymograph of the yellow dashed line in b), scalebars are 5µm (horizontal) and 10s (vertical). (d) Exemplary linescan intensity (normalized) for conditions in e. (e) Bundling metric λ of fascin and α-actinin crosslinked networks as well as F-actin network without crosslinkers. N = 3 for each condition. (f) Exemplary autocorrelation function of actin network fluctuations as function of lag time Δt. (g) Characteristic time τ for different conditions. N = 5,3,3,3,3,3 respectively. (h) Confocal fluorescence microscopy image of 2D actomyosin network crosslinked by fascin (top) and α-actinin (bottom) deformed and contracted under myosin active stress over time. Scalebars are 20 µm. Heatmaps show accumulative strain of the final frame. Quiver plot overlay shows the instantaneous velocity. (i) Kymograph of α-actinin network rupture (dashed red line in h). Scalebars are 10µm and 10s. (j) Mean strain $< \varepsilon >$ of the network during deformation caused by myosin induced active stress over time. The slope of the strain curve is the strain rate $\frac{d\varepsilon}{dt}$. (k) Maximum mean strain $< \varepsilon >_{max}$ of fascin and α-actinin crosslinked networks at $R_c = 0.2$. N = 3 for each condition. $p_{fas-aa} = 0.0101$. (l) Strain rate $\frac{d\varepsilon}{dt}$ of the network crosslinked by α-actinin at $R_c = 0.1$ at various myosin concentrations. N = 2,3,3,3,2,2,2 from low to high concentration respectively.

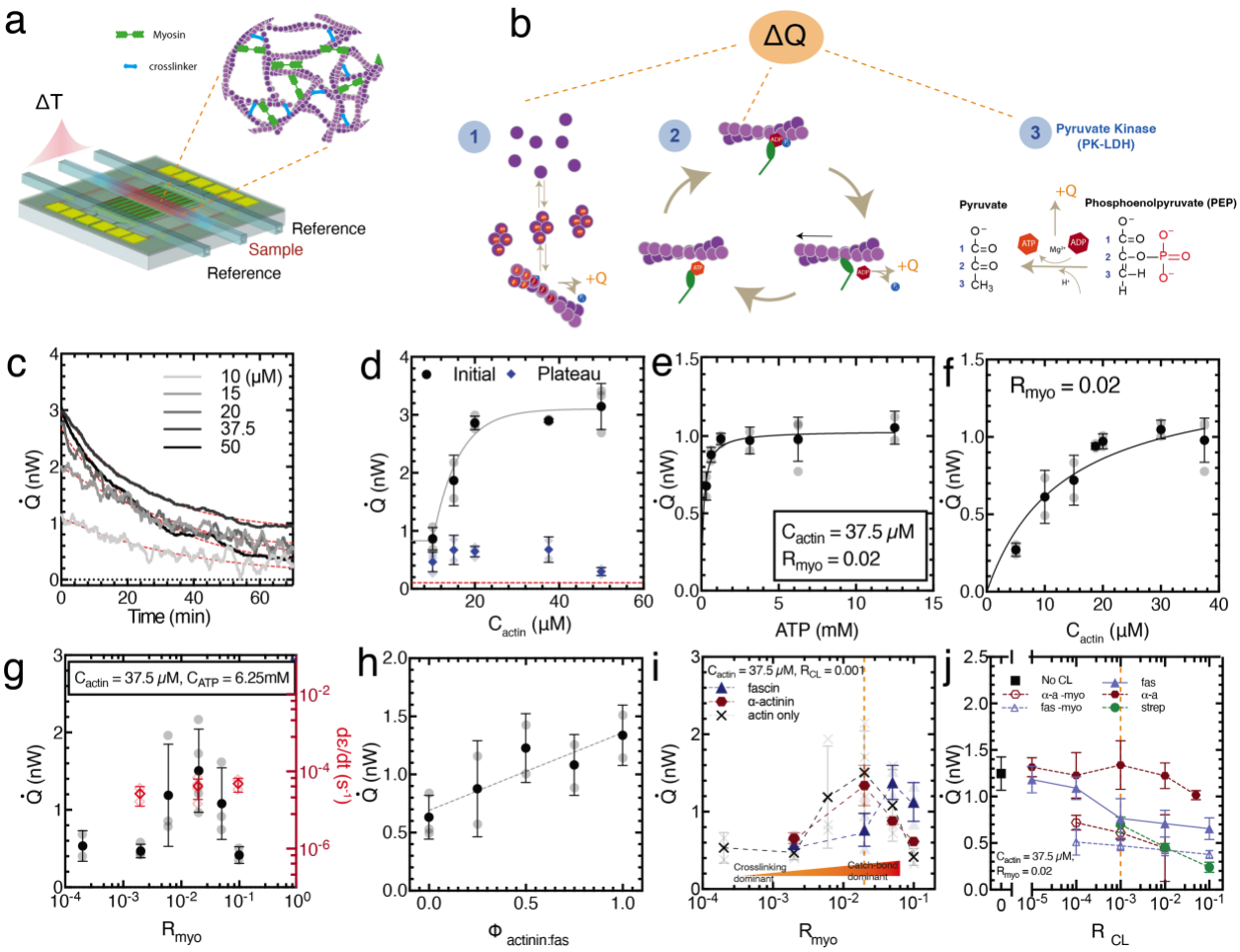

Fig. 2. **Catch- and slip-bond crosslinkers tune non-monotonic heat dissipation generated by the actomyosin crossbridge.** (a) Schematic of calorimeter and the zoomed-in circle shows the actomyosin sample details in the capillary tube that contains the sample. (b) Schematic of ATPase activities from 1. actin polymerization; 2. myosin ATPase in the network; and 3. the chemical reaction of ATP regeneration system via Pyruvate assay. (c) Heat dissipation rate ($\dot{Q}$) of actin polymerization at various actin concentrations over time. (d) Initial (black circles) and steady state (blue diamonds) heat dissipation rate ($\dot{Q}$) at various actin concentrations. Gray line is a Michaelis-Menten curve fit. (e) Heat dissipation rate of actomyosin network at various ATP concentrations (C_{actin} = 37.5μM, R_{myo} = 0.02.) Black line is the fit of Michaelis-Menten curve to data. (f) Heat dissipation rate of actomyosin network at various actin concentrations (R_{myo} = 0.02.) Black line is the fit of Michaelis-Menten curve to data. (g) Heat dissipation rate ($\dot{Q}$)of actomyosin network at various myosin-to-actin ratios (C_{actin} = 37.5μM, C_{ATP} = 6.25mM.) (h) Heat dissipation rate ($\dot{Q}$) of actomyosin network under same crosslinking ratio R_{CL} = 0.001 but at different α-actinin:fascin ratios ($\Phi_{actin:fascin}$). Gray dashed line is a linear fit to the data. (i) Heat dissipation rate ($\dot{Q}$) of actomyosin network under same crosslinking ratio R_{CL} = 0.001and C_{actin} = 37.5μM, at various R_{myo}. (j) Heat dissipation rate ($\dot{Q}$) of actomyosin network at R_{myo} = 0.02, C_{actin} = 37.5μM, and various crosslinking ratio R_{CL}.

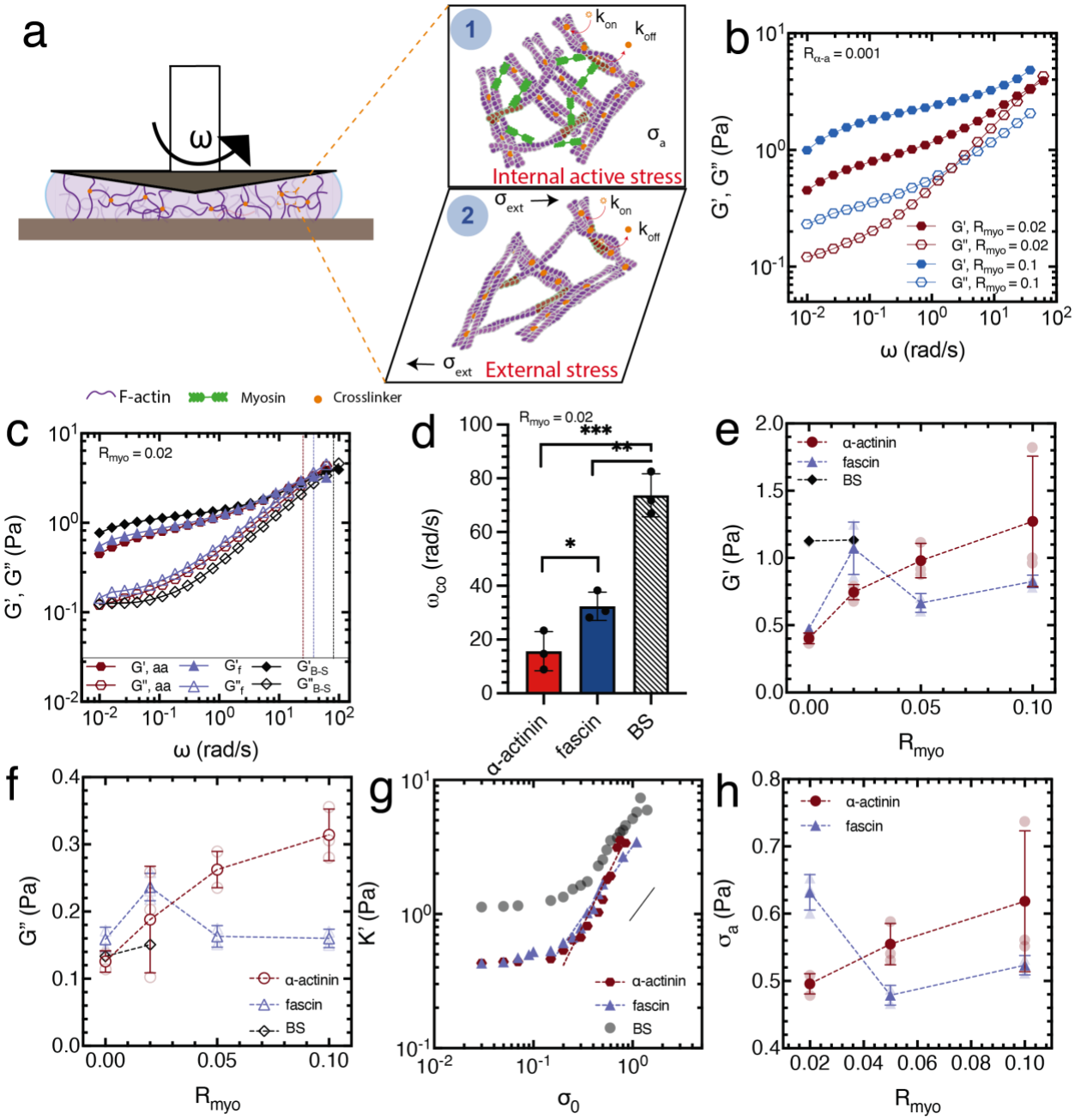

Fig. 3 Rheological mapping reveals delocalized active stress in catch-bonded networks. (a) Schematic of crosslinked network inside a cone-and-plate rheometer for (1) under active stress (top right) and (2) under rheometer-induced prestress (bottom right). (b) Frequency sweep (G', elastic modulus, and G'', viscous modulus) of the α-actinin crosslinked network (R_{CL} = 0.001) under active stress induced by myosin (R_{myo} = 0.02, maroon, and 0.1, blue). (c) Frequency sweep (G', elastic modulus, and G'', viscous modulus) of the α-actinin (maroon hexagons), fascin (blue triangles), and biotin-streptavidin (black diamonds) crosslinked networks. Vertical dashed lines indicate the G' and G'' crossover frequency ω_{co} for three cases. (d) Crossover frequency ω_{co} for the three conditions in (c). (e) Elastic modulus G' of the three types of network with various R_{myo}. (f) Viscous modulus G'' of the three types of network with various R_{myo}. (g) Differential elastic

modulus K' for the three types of networks as a function of prestress σ_0. Black line is indicative of slope of 1. (h) Indicated active stress σ_a as a function of R_{myo} for the three types of networks.

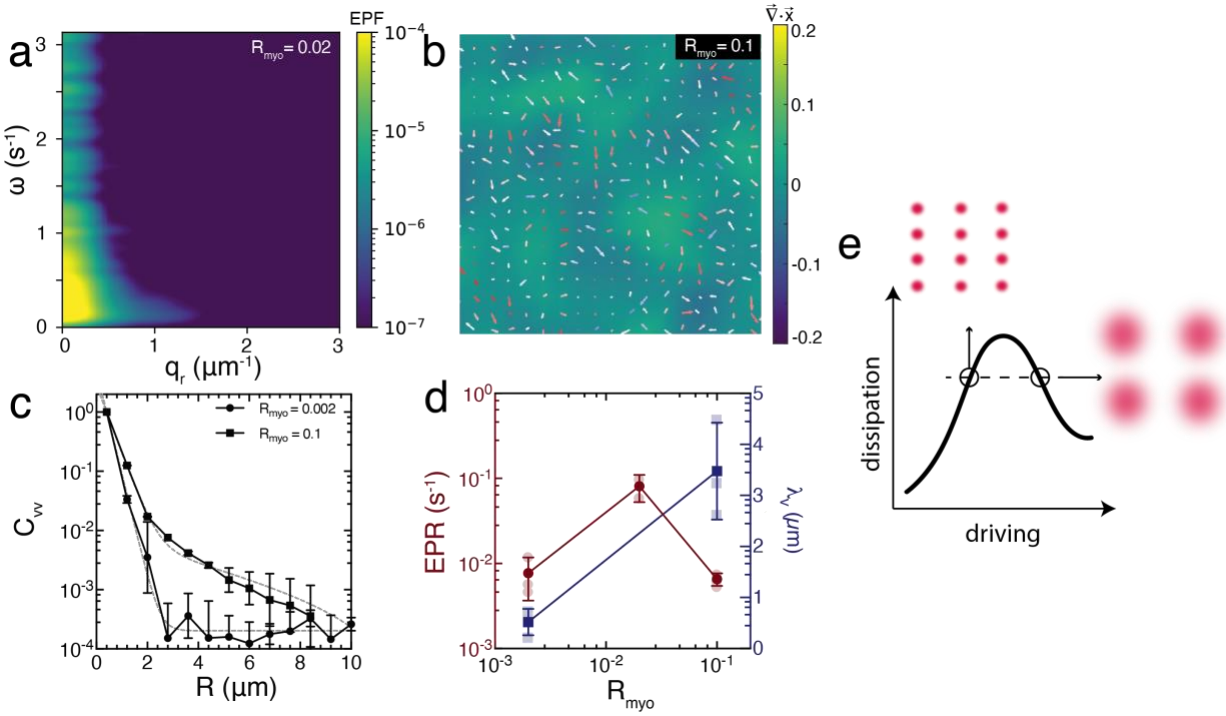

Fig. 4. Degeneracy in dissipation emerges from stress localization and delocalization . (a) Heat map of azimuthally averaged Entropy Production Factor (EPF) as a function of frequency (ω) and wave vector (q_r). R_{myo} = 0.02. (b) Heatmap shows accumulative strain (colorbar) after 5 minutes of completion of polymerization. Quiver plot overlay shows the mean velocity within the 5 minutes. Arrow color indicates the degree of alignment of the velocity with its neighbors. Red-white-blue indicates 'highly aligned'- 'not aligned' – 'anti-aligned'. R_{myo} = 0.1. (c) Azimuthally averaged velocity spatial correlation (C_{vv}) as a function of radius R. N = 3 for both cases. Errorbars are the s.t.d. of the mean. Gray dashed lines are the exponential fit. (d) Entropy Production Rate (EPR, maroon, left y-axis) and characteristic length (λ_v, blue, right y-axis) as a function of R_{myo}. N = 3 for all conditions. Errorbars are the s.t.d. of the mean. (e) Schematic of how degeneracy in dissipation can arise from the two ends of the driving due to stress de/localization.

Acknowledgments

We are grateful for insightful discussions with Dr. Daniel Needleman and Dr. Peter Foster. Z.G.S. acknowledges fundings and support from Yale PEB, his family, and friends during his exchange period at Harvard. This work was supported by funding ARO MURI W911NF-14-1-0403, the National Institutes of Health (NIH) R01 GR130179, Sloan Matter-to-Life G-2025-79182 , and Human Frontiers Science Program (HFSP) grant number RGP012/2025 to M.P.M.

Author Contributions

Z.G.S. & M.P.M designed and conceived the work. Z.G.S. & M.P.M. drafted the paper. Z.G.S, M.P.M, & J.J.V. edited the paper. Z.G.S. and A.P.T. performed experiments. Z.G.S. analyzed the data. J.Z. instructed on calorimeter operation. Z.G.S, M.P.M, J.J.V., & J.Z. participated in the discussion of the work. M.P.M. & J.J.V. supervised the work.

Competing Interests

A patent, entitled as "Microcalorimetry for high-throughput screening of bioenergetics", has been filed for the devices by Harvard University (inventors: J. Zheng, J.J. Vlassak, D.J. Needleman).

References

1 Onsager, L. Reciprocal relations in irreversible processes. II. *Physical Review* **38**, 2265-2279 (1931). https://doi.org:DOI 10.1103/PhysRev.38.2265

2 Onsager, L. Reciprocal relations in irreversible processes. I. *Physical Review* **37**, 405-426 (1931). https://doi.org:DOI 10.1103/PhysRev.37.405

3 Seifert, U. Stochastic thermodynamics, fluctuation theorems and molecular machines. *Rep Prog Phys* **75**, 126001 (2012). https://doi.org:10.1088/0034-4885/75/12/126001

4 Battle, C. *et al.* Broken detailed balance at mesoscopic scales in active biological systems. *Science* **352**, 604-607 (2016). https://doi.org:10.1126/science.aac8167

5 Mizuno, D., Tardin, C., Schmidt, C. F. & Mackintosh, F. C. Nonequilibrium mechanics of active cytoskeletal networks. *Science* **315**, 370-373 (2007). https://doi.org:315/5810/370 [pii]
10.1126/science.1134404

6 Onsager, L. Reciprocal relations in irreversible processes. I. *Physical review* **37**, 405 (1931).

7 De Groot, S. R. & Mazur, P. *Non-equilibrium thermodynamics*. (Courier Corporation, 2013).

8 Prigogine, I. & Van Rysselberghe, P. Introduction to thermodynamics of irreversible processes. *Journal of The Electrochemical Society* **110**, 97C (1963).

9 Chaikin, P. M., Lubensky, T. C. & Witten, T. A. *Principles of condensed matter physics*. Vol. 10 (Cambridge university press Cambridge, 1995).

10 Seifert, U. Stochastic thermodynamics, fluctuation theorems and molecular machines. *Reports on progress in physics* **75**, 126001 (2012).

11 Kubo, R. Statistical-Mechanical Linear Response Theory of Irreversible Processes. *P Jpn Acad* **45**, R11-& (1969).

12 Cross, M. C. & Hohenberg, P. C. Pattern-Formation Outside of Equilibrium. *Rev Mod Phys* **65**, 851-1112 (1993). https://doi.org:DOI 10.1103/RevModPhys.65.851

13 Julicher, F., Kruse, K., Prost, J. & Joanny, J. F. Active behavior of the cytoskeleton. *Physics Reports-Review Section of Physics Letters* **449**, 3-28 (2007). https://doi.org:10.1016/j.physrep.2007.02.018

14 Kruse, K., Joanny, J. F., Julicher, F., Prost, J. & Sekimoto, K. Asters, vortices, and rotating spirals in active gels of polar filaments. *Phys Rev Lett* **92** (2004). https://doi.org:ARTN 078101
10.1103/PhysRevLett.92.078101

15 Prost, J. Physics of active gels. *Abstr Pap Am Chem S* **230**, U3582-U3582 (2005).

16 Prost, J., Julicher, F. & Joanny, J. F. Active gel physics. *Nat Phys* **11**, 111-117 (2015). https://doi.org:10.1038/Nphys3224

17 Tabatabai, A. P. *et al.* Detailed Balance Broken by Catch Bond Kinetics Enables Mechanical-Adaptation in Active Materials. *Advanced Functional Materials* **n/a**, 2006745 https://doi.org:https://doi.org/10.1002/adfm.202006745

18 Marshall, B. T. *et al.* Direct observation of catch bonds involving cell-adhesion molecules. *Nature* **423**, 190-193 (2003). https://doi.org:10.1038/nature01605

19 Thomas, W. E., Vogel, V. & Sokurenko, E. Biophysics of catch bonds. *Annu Rev Biophys* **37**, 399-416 (2008). https://doi.org:10.1146/annurev.biophys.37.032807.125804

20 Kong, F., García, A. J., Mould, A. P., Humphries, M. J. & Zhu, C. Demonstration of catch bonds between an integrin and its ligand. *J Cell Biol* **185**, 1275-1284 (2009). https://doi.org:10.1083/jcb.200810002

21 Mulla, Y. *et al.* Weak catch bonds make strong networks. *Nature materials* **21**, 1019-1023 (2022).

22 Murrell, M. P. & Gardel, M. L. F-actin buckling coordinates contractility and severing in a biomimetic actomyosin cortex. *Proceedings of the National Academy of Sciences* **109**, 20820-20825 (2012).

23 Koenderink, G. H. *et al.* An active biopolymer network controlled by molecular motors. *Proceedings of the National Academy of Sciences* **106**, 15192-15197 (2009).

24 Humphrey, D., Duggan, C., Saha, D., Smith, D. & Käs, J. Active fluidization of polymer networks through molecular motors. *Nature* **416**, 413-416 (2002).

25 Mizuno, D., Tardin, C., Schmidt, C. F. & MacKintosh, F. C. Nonequilibrium mechanics of active cytoskeletal networks. *Science* **315**, 370-373 (2007).

26 Bendix, P. M. *et al.* A quantitative analysis of contractility in active cytoskeletal protein networks. *Biophysical journal* **94**, 3126-3136 (2008).

27 Sokurenko, E. V., Vogel, V. & Thomas, W. E. Catch-bond mechanism of force-enhanced adhesion: counterintuitive, elusive, but… widespread? *Cell host & microbe* **4**, 314-323 (2008).

28 Xu, X.-P. *et al.* Structural basis of αE-catenin–F-actin catch bond behavior. *Elife* **9**, e60878 (2020).

29 Wang, A., Dunn, A. R. & Weis, W. I. Mechanism of the cadherin–catenin F-actin catch bond interaction. *Elife* **11**, e80130 (2022).

30 Thomas, W. E., Vogel, V. & Sokurenko, E. Biophysics of catch bonds. *Annu. Rev. Biophys.* **37**, 399-416 (2008).

31 Evans, E. & Ritchie, K. Dynamic strength of molecular adhesion bonds. *Biophysical journal* **72**, 1541-1555 (1997).

32 Merkel, R., Nassoy, P., Leung, A., Ritchie, K. & Evans, E. Energy landscapes of receptor–ligand bonds explored with dynamic force spectroscopy. *Nature* **397**, 50-53 (1999).

33 Seara, D. S. *et al.* Entropy production rate is maximized in non-contractile actomyosin. *Nature communications* **9**, 4948 (2018).

34 Chen, S. *et al.* Energy partitioning in the cell cortex. *Nature Physics* **20**, 1824-1832 (2024).

35 Murrell, M., Thoresen, T. & Gardel, M. Reconstitution of contractile actomyosin arrays. *Methods Enzymol* **540**, 265-282 (2014). https://doi.org:10.1016/B978-0-12-397924-7.00015-7

36 Murrell, M. P. & Gardel, M. L. F-actin buckling coordinates contractility and severing in a biomimetic actomyosin cortex. *Proc Natl Acad Sci U S A* **109**, 20820-20825 (2012). https://doi.org:10.1073/pnas.1214753109

37 Murrell, M. & Gardel, M. L. Actomyosin Sliding is Attenuated in Contractile Biomimetic Cortices. *Mol Biol Cell* (2014). https://doi.org:10.1091/mbc.E13-08-0450

38 Sun, Z. G. *et al.* Cofilin-mediated actin filament network flexibility facilitates 2D to 3D actomyosin shape change. *European journal of cell biology* **103**, 151379 (2024).

39 Sun, Z. G. & Murrell, M. Cofilin-Mediated Filament Softening and Crosslinking Counterbalance to Enhance Actin Network Flexibility. *Physical Review Letters* **133**, 218402 (2024).

40 Luan, Y., Lieleg, O., Wagner, B. & Bausch, A. R. Micro-and macrorheological properties of isotropically cross-linked actin networks. *Biophysical journal* **94**, 688-693 (2008).

41 Lieleg, O., Claessens, M. M., Heussinger, C., Frey, E. & Bausch, A. R. Mechanics of bundled semiflexible polymer networks. *Physical review letters* **99**, 088102 (2007).

42 Lieleg, O., Claessens, M. M. & Bausch, A. R. Structure and dynamics of cross-linked actin networks. *Soft Matter* **6**, 218-225 (2010).

43 Cocconi, L., Chatzittofi, M. & Golestanian, R. Mechanical inhibition of dissipation in a thermodynamically consistent active solid. *arXiv preprint arXiv:2506.18000* (2025).

44 Pollard, T. D. Rate constants for the reactions of ATP-and ADP-actin with the ends of actin filaments. *The Journal of cell biology* **103**, 2747-2754 (1986).

45 Baker, J. E., Brosseau, C., Joel, P. B. & Warshaw, D. M. The biochemical kinetics underlying actin movement generated by one and many skeletal muscle myosin molecules. *Biophysical journal* **82**, 2134-2147 (2002).

46 Stewart, T. J., Murthy, V., Dugan, S. P. & Baker, J. E. Velocity of myosin-based actin sliding depends on attachment and detachment kinetics and reaches a maximum when myosin-binding sites on actin saturate. *Journal of Biological Chemistry* **297** (2021).

47 Resnicow, D. I., Deacon, J. C., Warrick, H. M., Spudich, J. A. & Leinwand, L. A. Functional diversity among a family of human skeletal muscle myosin motors. *Proceedings of the National Academy of Sciences* **107**, 1053-1058 (2010).

48 Haldeman, B. D., Brizendine, R. K., Facemyer, K. C., Baker, J. E. & Cremo, C. R. The kinetics underlying the velocity of smooth muscle myosin filament sliding on actin filaments in vitro. *Journal of Biological Chemistry* **289**, 21055-21070 (2014).

49 Finer, J. T., Simmons, R. M. & Spudich, J. A. Single myosin molecule mechanics: piconewton forces and nanometre steps. *nature* **368**, 113-119 (1994).

50 Sweeney, H. L. & Houdusse, A. Structural and functional insights into the myosin motor mechanism. *Annual review of biophysics* **39**, 539-557 (2010).

51 Johnson, C. A. *et al.* The ATPase cycle of human muscle myosin II isoforms: Adaptation of a single mechanochemical cycle for different physiological roles. *Journal of Biological Chemistry* **294**, 14267-14278 (2019).

52 Geeves, M. A. & Holmes, K. C. The molecular mechanism of muscle contraction. *Advances in protein chemistry* **71**, 161-193 (2005).

53 Kovács, M., Thirumurugan, K., Knight, P. J. & Sellers, J. R. Load-dependent mechanism of nonmuscle myosin 2. *Proceedings of the National Academy of Sciences* **104**, 9994-9999 (2007).

54 Soares e Silva, M. *et al.* Active multistage coarsening of actin networks driven by myosin motors. *Proceedings of the National Academy of Sciences* **108**, 9408-9413 (2011).

55 Ruiz-Franco, J., Tauber, J. & van der Gucht, J. Cross-linker mobility governs fracture behavior of catch-bonded networks. *Physical Review Letters* **130**, 118203 (2023).

56 Broedersz, C. & MacKintosh, F. Molecular motors stiffen non-affine semiflexible polymer networks. *Soft Matter* **7**, 3186-3191 (2011).

57 Shin, J. H., Gardel, M., Mahadevan, L., Matsudaira, P. & Weitz, D. Relating microstructure to rheology of a bundled and cross-linked F-actin network in vitro. *Proceedings of the National Academy of Sciences* **101**, 9636-9641 (2004).

58 Gardel, M. L. *et al.* Elastic behavior of cross-linked and bundled actin networks. *Science* **304**, 1301-1305 (2004).

59 Gardel, M. L. *et al.* Prestressed F-actin networks cross-linked by hinged filamins replicate mechanical properties of cells. *Proceedings of the National Academy of Sciences* **103**, 1762-1767 (2006).
60 Seara, D. S., Machta, B. B. & Murrell, M. P. Irreversibility in dynamical phases and transitions. *Nature communications* **12**, 392 (2021).
61 Callen, H. B. Thermodynamics and an Introduction to Thermostatistics. *John Wiley& Sons* **2** (1993).
62 Marchetti, M. C. *et al.* Hydrodynamics of soft active matter. *Reviews of modern physics* **85**, 1143-1189 (2013).
63 Jülicher, F., Grill, S. W. & Salbreux, G. Hydrodynamic theory of active matter. *Reports on Progress in Physics* **81**, 076601 (2018).
64 Foster, P. J. *et al.* Dissipation and energy propagation across scales in an active cytoskeletal material. *Proceedings of the National Academy of Sciences* **120**, e2207662120 (2023).
65 Anderson, P. W. Absence of diffusion in certain random lattices. *Physical review* **109**, 1492 (1958).
66 Sun, Z. G. *et al.* Feedback between F-actin organization and active stress governs criticality and energy localization in the cell cytoskeleton. *Nature Physics*, 1-13 (2025).
67 Strogatz, S. H. *Nonlinear dynamics and chaos: with applications to physics, biology, chemistry, and engineering*. (Chapman and Hall/CRC, 2024).
68 J Evans, D. & P Morriss, G. *Statistical mechanics of nonequilbrium liquids*. (ANU Press, 2007).
69 Gnesotto, F. S., Mura, F., Gladrow, J. & Broedersz, C. P. Broken detailed balance and non-equilibrium dynamics in living systems: a review. *Reports on Progress in Physics* **81**, 066601 (2018).
70 De Gennes, P.-G. *Superconductivity of metals and alloys*. (CRC press, 2018).
71 Tinkham, M. *Introduction to superconductivity*. (Courier Corporation, 2004).
72 Cross, M. C. & Hohenberg, P. C. Pattern formation outside of equilibrium. *Reviews of modern physics* **65**, 851 (1993).
73 Bardeen, J., Cooper, L. N. & Schrieffer, J. R. Theory of superconductivity. *Physical review* **108**, 1175 (1957).

570
571 **Methods**

572 **Preparation of small unilamellar vesicles (SUVs)**

573 Lipids were combined by mixing 100 µL of egg phosphatidylcholine (Egg PC, 25 mg mL^{-1}; Avanti
574 Polar Lipids, 840051C) with 10 µL of 1,2-dihexadecanoyl-sn-glycero-3-phosphoethanolamine
575 (DHPE, 0.5 mg mL^{-1}), optionally conjugated to Oregon Green 488 (Invitrogen). All lipids were
576 dissolved in chloroform and transferred to a clean glass vial pre-equilibrated with argon to
577 minimize oxidative degradation. The solvent was removed under a gentle stream of argon, yielding
578 a uniform lipid film coating the bottom of the vial. The dried lipid film was rehydrated with 5 mL
579 of vesicle buffer (100 mM NaCl, 20 mM HEPES, pH 7.5) and vortexed until the suspension
580 became turbid. The dispersion was then sonicated in a bath sonicator for approximately 1 h, or
581 until the solution turned optically clear, indicating the formation of small unilamellar vesicles
582 suitable for bilayer formation.

583 **Fluorescent labeling of skeletal muscle myosin**
584 Skeletal muscle myosin (Heavy Meromyosin from rabbit, Cytoskeleton Inc.) is fluorescently
585 labeled with Alexa Fluor 647 C2 Maleimide under reducing conditions. Initially, myosin is
586 reduced in a labeling buffer containing 50 mM HEPES, 0.5 M KCl, 1 mM EDTA, and 10 mM
587 DTT at pH 7.6. Following reduction, the sample is dialyzed overnight against the same buffer
588 without DTT. After dialysis, the solution is centrifuged to eliminate any insoluble components.
589 The resulting supernatant is reacted with Alexa Fluor C2 Maleimide at a 5:1 molar ratio of dye to
590 myosin. Labeling is carried out at 4°C for one hour, after which the reaction is quenched by adding
591 1 mM DTT. The labeled protein is purified using a desalting column (Pierce, 5K MWCO, 5 mL).
592 Absorbance readings at 280 nm and 647 nm are then used to calculate the degree of labeling. This
593 protocol is adapted from Verkohovsky and Borisy[1].
594
595 **2D actomyosin contraction experiments**
596 Each chamber is of cylindrical shape, with diameter of 12mm. The top and bottom piece are
597 magnetically locked, with a rubber piece sealing the middle and a glass slide sandwiched in
598 between. The glass slide is first washed with 50% ethanol to clean any residues left on the surface.
599 The slide is then exposed under UV light for 5 min to induce hydrophilicity to the surface. 300 µL
600 of SUV solution is added to the chamber. Once the surface of the glass is coated with lipid bilayer,
601 we take 100 µL solution out and wash the chamber with 400 µL of 1x F-buffer (10 mM imidazole,
602 1 mM $MgCl_2$, 50 mM KCl, 2 mM EGTA, 0.5 mM ATP, pH = 7.5). Dark G-actin (Cytoskeleton)
603 is mixed with rhodamine labelled F-actin (20% fluorescent, Cytoskeleton) to a final molar
604 concentration of 1.4 µM, and is stabilized with 1 µM phalloidin (Cytoskeleton) and crowded to the
605 surface of a 97% Egg Phosphatidyl Choline (Avanti Polar Lipids)/3% FITC-DHPE (Molecular
606 Probes) phospholipid bilayer, using 0.2% 14,000 MW methyl-cellulose (Sigma, 15 cP) as a
607 depletion agent (Fig. 1A). The actin mixed soup is placed in an Eppendorf tube on ice for 1 hour
608 to reach full polymerization (50 µL protein mix in total). Once F-actin is polymerized, it is added
609 to the chamber, along with methyl-cellulose. Once the F-actin network is crowded onto the surface,
610 we add crosslinkers α-actinin or fascin of various concentrations. Then, Skeletal muscle myosin
611 II (various concentrations), labelled with Alexa Flour 647nm C2 Maleimide (Molecular Probes) is

added in solution in dimeric form, which polymerizes into thick filaments onto the F-actin. This results in a two-dimensional actomyosin network.

Removing non-catalytically active skeletal muscle myosin

To isolate only catalytically active myosin dimers for experimental use, myosin is subjected to a selective centrifugation process in the presence of polymerized actin. First, actin is polymerized for one hour at 4°C in a high-salt environment (1X F-buffer supplemented with 4 M KCl) and stabilized using phalloidin. After polymerization, ATP is added to reach a final concentration of 1 mM, followed by the addition of freshly thawed myosin. This actin-myosin mixture is incubated at 4°C for 10 minutes, then centrifuged at 128,360 × g for 30 minutes. During centrifugation, enzymatically inactive myosin remains bound to the F-actin network and sediments, while active myosin motors detach and remain in the supernatant, which is then collected. The concentration of active myosin in the supernatant is quantified by measuring absorbance at 647 nm, based on a pre-determined labeling efficiency. Myosin is freshly prepared for each experiment and used within 24 hours.

Microscopy

The image stack data are collected using Leica DMi8 inverted microscope equipped with a 63×, 40×, or 20×, and 1.4, 1.3, and 0.75-NA oil immersion lens respectively (Leica Microsystems), a spinning-disk confocal (CSU22; Yokagawa), and sCMOS camera (Zyla; Andor Technology) controlled by Andor iQ3 (Andor Technology). Image time series stack data are taken with time interval of 0.5-10 seconds.

Picocalorimetry Measurements

Metabolic heat was quantified using a custom micromachined capillary-based picocalorimetry system, as previously described (Zheng et al.). Three borosilicate glass capillaries (400 µm × 400 µm outer dimension, 100 µm wall thickness) were bonded onto gold-coated regions of a silicon-nitride membrane integrating two Nichrome/Constantan thermopiles and a tungsten micro-heater. One capillary was loaded with the biological sample, and two identical capillaries containing pure water served as thermal references. Heat generated by the sample produced a temperature differential relative to the references, which was converted into a voltage by the thermopiles through the Seebeck effect. The monitored sensing volume within the sample capillary was ~80 nL.

The calorimeter assembly was mounted on a custom PCB and placed inside a thermally insulated vacuum chamber evacuated to ~10^{-5} Torr to suppress convective heat loss and reduce electrical noise. Measurements were performed at 25 °C. Thermopile voltages were acquired using two Keithley 2182A nanovoltmeters operated at 6 PLC with power-line synchronization and auto-zero enabled. Data were sampled at 2.31 Hz and processed using a moving-average filter. Under these measurement conditions, the system exhibited an effective noise floor corresponding to a power sensitivity of ~85 pW.

Experimental setup and procedures for rheology experiments

Rheological measurements of actin networks were performed using a stress-controlled rheometer (Anton Paar M502). Actin was first prepared following the composition detailed in Table 1, and the final sample mixture (Table 2) was assembled to a total volume of 1000 µL. After gentle mixing, the solution was loaded onto the preheated bottom plate maintained at 25 °C. Both the

cone and plate surfaces were sandblasted to prevent sample slippage. Following equilibration, several drops of silicone oil were added around the sample edge to minimize evaporation, and a solvent trap was placed over the geometry for additional protection. Gelation kinetics were monitored under the parameters described in the main text. After gelation reached a steady plateau in both elastic (G′) and viscous (G″) moduli (typically after ~2 h), measurements in the linear and nonlinear regimes were performed. After each experiment, the setup was thoroughly cleaned with sequential rinses of 70% ethanol, water, ethanol, and water to ensure complete removal of residual protein and prevent cross-contamination between runs.

Experimental setup and procedures for microscopy experiments

Unlabeled rabbit skeletal muscle actin (>99% purity; Cytoskeleton, Inc.)—hereafter referred to as dark actin—was reconstituted in 1× G-buffer (see Table 3) to a concentration of 10 mg mL^{-1}. Rhodamine-labeled actin (Cytoskeleton, Inc.) was prepared using the same procedure. Both preparations were depolymerized for over 24 h at 4 °C in the dark (see Table 3). The two actin species were then mixed at a 9:1 ratio (dark:rhodamine) to yield G-actin. Polymerization was initiated by combining the protein mixture with polymerization buffer (Table 4). Glucose oxidase, catalase (GOC), and glucose were added as an oxygen scavenging system to minimize photobleaching during imaging.

Samples were loaded into a custom four-well round chamber, each well comprising a cylindrical cavity sealed by a 12 mm glass coverslip and a rubber spacer to prevent leakage. Coverslips were sequentially cleaned with 70% ethanol, dried, and exposed to UV light for 5 min to render the surface hydrophilic. To reduce actin adsorption, surfaces were coated with small unilamellar vesicles (SUVs; protocol available upon request). After gentle mixing (30 s), 200 µL of the protein mixture was injected into each well. Samples were imaged using a Leica confocal microscope (see *Microscopy* section).

ATP-regeneration system

ATP regeneration system was used in all experiments, containing ATP at the indicated concentrations (0.625–12.5 mM), 40 mM phosphoenolpyruvate (PEP), and a coupled pyruvate kinase/lactate dehydrogenase (PK/LDH) enzyme mixture (Sigma-Aldrich). The PK/LDH enzymes were mixed at a 1:1 ratio (1 mg mL^{-1} stock concentration), and 2.5 µL of the enzyme mixture was added per reaction volume of 800 µL.

Particle Image Velocimetry (PIV)

Particle image velocimetry (PIV) is applied on the fluorescent actin images in MATLAB (mPIV, https://www.mn.uio.no/math/english/people/aca/jks/matpiv/). The extent of contraction is calculated by defining a mean strain:

$$< \varepsilon > = < \vec{\nabla} \cdot \vec{\mathbf{x}}_{\mathbf{c}} > \quad (1)$$

, as the divergence of the displacement field. The data is analyzed with PIV window size 32 and overlap 0.5. Window size of 16 and 64 have also been used to generate the data, and eventually determined that 32 is the best parameter value because of the high signal-to-noise ratio.

2D image thresholding method for calculating bundling parameter

For each microscopy image of F-actin network, a line scan of approximately 20 μm is done to the image and the fluorescence intensity is extracted from the line scan. The bundling parameter λ is calculated using the equation:

$$\lambda = \nu/\mu \tag{2}$$

, in which ν is the standard deviation of the fluorescence intensity of the line scan, and μ the mean of the fluorescence intensity of the same line scan.

Autocorrelation analysis

After the F-actin network reached a steady state, time-lapse fluorescence image sequences were acquired with randomly chosen starting times. To quantify the temporal dynamics of the network at the global level, we computed the traditional temporal autocorrelation of the fluorescence intensity using custom MATLAB scripts.

For each frame, the fluorescence intensity was spatially averaged over all pixels in the image, yielding a single intensity time series $I(t)$. The mean intensity $\langle I \rangle$was then subtracted to isolate temporal fluctuations, $\delta I(t) = I(t) - \langle I \rangle$. The normalized temporal autocorrelation function was calculated according to

$$C(\Delta t) = \frac{\langle \delta I(t)\, \delta I(t + \Delta t) \rangle_t}{\langle \delta I(t)^2 \rangle_t} \tag{3}$$

where $\langle \cdot \rangle_t$denotes an average over all valid time points separated by a delay Δt. This normalization ensures $C(0) = 1$. Because the number of statistically independent pairs decreases with increasing delay time, the autocorrelation at large Δt is increasingly affected by finite-sampling noise and was not interpreted quantitatively.

The experimentally measured autocorrelation functions were fit using a double-exponential decay model,

$$C(\Delta t) = a\, \mathrm{e}^{-\Delta t/\tau_1} + (1 - a)\, \mathrm{e}^{-\Delta t/\tau_2} \tag{4}$$

$$\tau = a\tau_1 + (1 - a)\, \tau_2 \tag{5}$$

where a and $1 - a$ are the relative amplitudes of the two relaxation modes, and $\tau_1$and $\tau_2$are their associated characteristic times. Fitting was restricted to the initial portion of the correlation curve (typically the first 30% of the available delay times), as long-lag data points are dominated by statistical uncertainty arising from finite acquisition length.

Mechanical power calculation using PIV velocity field

Defining $\eta'(\omega) = \frac{G''(\omega)}{\omega}$, this is:

$$\langle p \rangle = \int_0^\infty \eta'(2\pi f)\ S_{\dot{\gamma}}(f)\, df \tag{6}$$

For a 2D/3D velocity field, using the strain-rate tensor $D_{ij}(\vec{r}, t)$ and its PSDs:

$$\langle p \rangle \approx 2\beta \int_0^{f_{max}} \eta'(2\pi f)\ \left[S_{xx}(f) + S_{yy}(f) + 2S_{xy}(f)\right] df \tag{7}$$

For more details, please refer to Supplemental Materials.

Velocity spatial correlation analysis

Equal-time spatial velocity correlations were computed from particle image velocimetry (PIV) data using a custom MATLAB pipeline. The velocity correlation function was defined as

$$C_{vv}(r) = \frac{\langle \mathbf{v}(\mathbf{r}', t) \cdot \mathbf{v}(\mathbf{r}' + \mathbf{r}, t) \rangle_{\mathbf{r}'}}{\langle |\ \mathbf{v}(\mathbf{r}', t)\ | \rangle_{\mathbf{r}'}^2}, \tag{8}$$

where $\mathbf{v}(\mathbf{r}', t)$denotes the local velocity fluctuation at position $\mathbf{r}'$and time t, and $\langle \cdot \rangle_{\mathbf{r}'}$indicates spatial averaging over all interrogation windows.

Velocity fields in the $x$and $y$directions (v_x, v_y) were first preprocessed to handle missing values arising from PIV failures. NaN entries were replaced using MATLAB's fillmissing function with linear interpolation to ensure spatial continuity of the velocity field.

To compute the correlation efficiently and without directional bias, the calculation was performed in Fourier space. For each time point, the mean velocity was subtracted from the raw velocity field $\mathbf{v}_0(\mathbf{r}', t)$to obtain velocity fluctuations,

$$\mathbf{v}(\mathbf{r}', t) = \mathbf{v}_0(\mathbf{r}', t) - \langle \mathbf{v}_0(\mathbf{r}', t) \rangle_{\mathbf{r}'}. \tag{9}$$

The resulting field was then normalized by its spatial root-mean-square magnitude,

$$\mathbf{v}_{\text{norm}}(\mathbf{r}', t) = \mathbf{v}(\mathbf{r}', t) / \sqrt{\sum_{\mathbf{r}'} |\ \mathbf{v}(\mathbf{r}', t)\ |^2}. \tag{10}$$

A two-dimensional fast Fourier transform (FFT) was applied to the normalized velocity field, and the autocorrelation was obtained via inverse FFT of the power spectrum:

$$C_{vv}(\mathbf{r}) = \text{Re}\left[\text{fftshift}\left(\text{ifft2}\left(\hat{\mathbf{v}}_{\text{norm}}(\mathbf{k}, t)\ \hat{\mathbf{v}}_{\text{norm}}^*(\mathbf{k}, t)\right)\right)\right], \tag{11}$$

where $\hat{\mathbf{v}}_{\text{norm}}(\mathbf{k}, t)$denotes the Fourier-transformed velocity field and $*$ indicates complex conjugation. The fftshift operation was used to center the zero-frequency component.

The resulting two-dimensional correlation map was radially averaged using a custom radialavg routine to obtain $C_{vv}(r)$. The decay of the correlation function was quantified by fitting to a single-exponential form,

$$C_{vv}(r) = b_1 \exp\left(-r/\lambda_v\right) + b_2, \tag{12}$$

where λ_v defines the characteristic velocity correlation length.

Entropy production calculation

The entropy production factor (EPF) and entropy production rate (EPR) are:

$$EPF\ (\boldsymbol{q}, \omega) = \frac{1}{2}[C^{-1}(\boldsymbol{q}, -\omega) - C^{-1}(\boldsymbol{q}, \omega)]_{ij} C^{ji}(\boldsymbol{q}, \omega) \tag{13}$$

$$EPR\ = \int \frac{d\omega}{2\pi} \frac{d^2\boldsymbol{q}}{(2\pi)^2} EPF\ (\boldsymbol{q}, \omega) \tag{14}$$

, where $C^{ij}(\boldsymbol{q}, \omega)$ is the dynamic structure factor (for more derivations, please refer to Seara, Machta, and Murrell, 2021). The entropy calculation and analyses are carried out using customized Python script utilizing *frequent* and *freqentn* package developed by Dr. Daniel S. Seara (https://github.com/lab-of-living-matter/freqent/tree/epf_paper/freqent).

Data availability

Source data are provided with this paper. Raw data supporting the findings of this manuscript are available from the corresponding authors upon reasonable request. A reporting summary for this Article is available as a Supplementary Information file.

Code availability

Code supporting the findings of this manuscript are available from the corresponding authors upon reasonable request. A reporting summary for this Article is available as a Supplementary Information file.